Understanding the effect of phosphorous on the ion-irradiation behaviour of RPV model steels using atom probe tomography and nanoindentation

Deepak Sharma, Auriane Etienne, Ronan Henry, Cornelia Kaden, Mélanie Picot, Bertrand Radiguet

To cite this version:

Deepak Sharma, Auriane Etienne, Ronan Henry, Cornelia Kaden, Mélanie Picot, et al.. Understanding the effect of phosphorous on the ion-irradiation behaviour of RPV model steels using atom probe tomography and nanoindentation. Acta Materialia, 2024, 270, pp.119859. 10.1016/j.actamat.2024.119859 . hal-04519681

HAL Id: hal-04519681
https://hal.science/hal-04519681

Submitted on 3 Apr 2024

Understanding the effect of phosphorous on the ion-irradiation behaviour of RPV model steels using atom probe tomography and nanoindentation

Deepak Sharma[1, #, *], Auriane Etienne[1], Ronan Henry[1], Cornelia Kaden[2], Mélanie Picot[1], Bertrand Radiguet[1]

[1]Groupe de Physique des Matériaux, Université et INSA de Rouen, UMR CNRS 6634, Rouen, 76800, France

[2]Helmholtz-Zentrum Dresden-Rossendorf, Bautzner Landstraße 400, 01328 Dresden, Germany

[#]Current affiliation of the author: Materials Innovation Centre, School of Engineering, University of Leicester, Leicester LE1 7RH, UK

*Corresponding author's email address: ds809@leicester.ac.uk

https://doi.org/10.1016/j.actamat.2024.119859

Abstract

Understanding the formation of the embrittling Mn-Ni-Si (MNS)-rich clusters in reactor pressure vessel (RPV) steels is of economic, environmental, and safety importance. Hence we investigated the influence of phosphorous (P) on the formation of MNS-rich clusters in RPV model steels employing atom probe tomography and nanoindentation tests. The atom probe tomography results show that the average number density and volume fraction of clusters decrease slightly with an increase in the bulk P content; however, higher bulk P led to a slight increase in the average diameter of the clusters. A higher amount of bulk P led to higher Cu in the clusters; suggesting synergy between Cu and P. An increase in the irradiation hardening values was observed due to higher bulk P content. This is attributed to the stabilisation of the self-interstitial atoms (SIA) clusters by P. A higher recovery for the sample containing higher bulk P indicated that the SIA clusters dissolved after post-irradiation annealing.

Keywords Reactor pressure vessel steels; Irradiation effect; Atom probe tomography; Solute clustering; Hardening

1. Introduction

Nuclear power plants (NPPs) can help us achieve the ever-increasing electricity demand sustainably and cleanly. The reactor pressure vessel (RPV), which is an integral and irreplaceable part of NPP, suffers embrittlement due to neutron irradiation during service [1]. This limits the lifetime of the NPP. This also raises concerns over safety during core-damaging situations, such as pressurised thermal shock generated during an emergency core cooling [1]. Hence, a better understanding of this embrittlement behaviour is of economic, environmental, and safety importance.

The embrittlement of RPV steels can result from the formation of solute clusters, precipitates, matrix damage, and segregation of elements to dislocations and grain boundaries under neutron irradiation [2–4]. Cu was very early on recognised as the dominant element for embrittlement due to the formation of Cu-rich precipitates [5–9]. Therefore, the amount of residual Cu was reduced (< 0.1 wt %) for the next-generation RPV steels. However, in the 1990s, Pareige *et al.* [10], through their atom probe and field ion microscopy study, reported the formation of Mn-Ni-Si (MNS)-rich nanosized clusters at higher neutron fluence; leading to the embrittlement of low-Cu RPV steels. Since then, there have been many studies [8,9,11–20] that have reported the formation of MNS-rich clusters/precipitates and their impact on embrittlement.

These MNS-rich clusters also contain residual elements – Cu and P [17,18]. There are many studies [1,21–23] dedicated to understanding the role of Mn, Ni, and Si on the formation of MNS-rich clusters. However, the role of P is not yet clear. Lee *et al.* [24] reported that Ni does not have an exclusive influence on hardening-embrittlement if P levels are strictly controlled in RPV steels. Hence, it becomes important to understand if P plays any role in the formation of MNS-rich clusters. Most of the studies [25–29] dedicated to understanding the role of P on RPV embrittlement are centered around understanding the effect of segregation of P on grain boundaries. The embrittlement due to intergranular segregation of P is called non-hardening embrittlement as it does not lead to hardening; unlike in the case of MNS-rich cluster formation. However, Röder *et al.* [30], through their nanoindentation study, recently concluded that P does have an impact on the hardening behaviour of RPV steels. They concluded that the hardening was due to the stabilisation of the cascade remnants by P segregation. These stabilised cascade remnants are the self-interstitial atoms (SIA) clusters that serve as the sinks for the migrating point defects and ultimately act as the nucleation sites for the formation of MNS-rich clusters [31]. Bergner *et al.* [32], through their small-angle neutron scattering (SANS) and tensile test studies, also reported that a higher amount of P leads to a higher increase in yield stress after irradiation. However, these studies did not report detailed microstructural information, and all the quantified information from the SANS data was on a normalised scale. Information such as cluster compositions and the absolute values for cluster quantifications are missing – which are important for modifying the ductile-to-brittle transition temperature prediction models [33]. Gómez-Ferrer *et al.* [34] also reported that P atoms have a strong clustering tendency in ferritic/martensitic steel; due to their fast diffusing nature. Therefore, there is a need to explore the microstructural changes happening in RPV steels under irradiation due to the presence of different bulk P content.

Atom probe tomography (APT) is one such technique that can provide structural and compositional information at the nano level [35–38]. The availability of such data will not only be useful for designing the materials for next-generation nuclear reactors but will also be useful in determining the long-term operation of the already existing NPPs – which is one of the current requirements for sustaining nuclear power as a source of carbon-free energy [39].

Hence we have investigated the role of P on the ion-irradiation behaviour of the RPV model steels. Ion irradiation was used here to understand the behaviour of P on solute clustering and radiation hardening, and how P interacts with small defect clusters. Direct extrapolation of the observed microstructural evolution to neutron irradiation at the same dose should be considered with caution. The irradiated samples were also annealed to study the influence of P on the stability of SIA clusters. APT was used to collect detailed microstructural information. The obtained microstructural data were correlated with the nanoindentation data; to understand the influence of P on the hardening behaviour of RPV model steels.

2. Materials and methods

2.1. Materials

Two Japanese commercial-grade RPV model steels, namely JPB and JPC, were studied in this work. These steels were manufactured by Nippon Steels Corporation, Japan. Both unirradiated and irradiated conditions were explored for comparison purposes. The steels were in plate form and underwent the same final heat treatment: normalisation at 800 °C for 1 h with air cooling, followed by tempering at 670 °C for 80 min with subsequent air cooling. The nominal chemical compositions (in at %) of these steels are presented in Table 1. These are low-Cu steels that differ only in their P content. Mechanically polished (down to 1 µm diamond suspension) samples of size 10 mm × 10 mm × 1 mm were used in this work.

Table 1. Nominal chemical compositions (in at %) of RPV model steels that were used in this work.

Code	C	Mn	Si	Cr	Ni	Mo	V	P	Cu	Fe
JPB	0.92	1.43	0.51	0.16	0.78	0.31	0.01	0.030	0.009	Bal
JPC	0.83	1.46	0.53	0.16	0.77	0.31	0.01	0.013	0.009	Bal

2.2. Ion irradiation and post-irradiation annealing

The polished samples were ion-irradiated at the Ion Beam Center in Helmholtz-Zentrum Dresden-Rossendorf, Dresden, Germany. The samples were irradiated at 300 °C with Fe^{2+} ions having 5 MeV energy; yielding damage of 0.1 dpa at the depth of 500 nm. The irradiation was performed by scanning a focused ion beam normal to the polished surface. The flux was kept at 10^{11} $cm^{-2}.s^{-1}$ (with x and y scanning frequencies of about 1 kHz). The beam current, irradiation time, and exposure for irradiation were 100–120 nA, 1 h, and 2.66×10^{14} cm^{-2}, respectively. The fluence was calculated using the SRIM code [40] as per the procedure given in the reference [41] for quick damage calculation. The displacement energy for a pure Fe target was taken as 40 eV; as per ASTM standard E521. The damage and the implantation profiles can be seen in Fig. 1 (a). More details on the ion irradiation process can be seen in the reference [30].

To study the stability of the irradiation-induced SIA clusters and how it is influenced by P content, the irradiated samples, for both the model steels, were annealed in a tube furnace under vacuum. The post-irradiation annealing (PIA) treatments were performed in a pre-heated furnace maintained at 350 °C for the ageing period of 5 h. This was followed by air cooling to room temperature. The PIA was performed at 350 °C to avoid the dissolution of MNS-rich clusters during PIA. According to Wells *et al.* [42] the MNS-rich clusters remain stable even when annealed for a week at 350 °C – 375 °C; therefore, this temperature was chosen. The main idea here was to find the origin of the high hardening of P-rich steel (section 3.5). The unirradiated, irradiated, and post-irradiation-annealed samples will hereafter be labelled as per Table 2.

Table 2. The sample nomenclature for this work.

Sample ID	Condition
JPB_Unir	Higher P + unirradiated
JPB_Ir	Higher P + irradiated
JPB_PIA	Higher P + irradiated + annealed
JPC_Unir	Lesser P + unirradiated
JPC_Ir	Lesser P + irradiated
JPC_PIA	Lesser P + irradiated + annealed

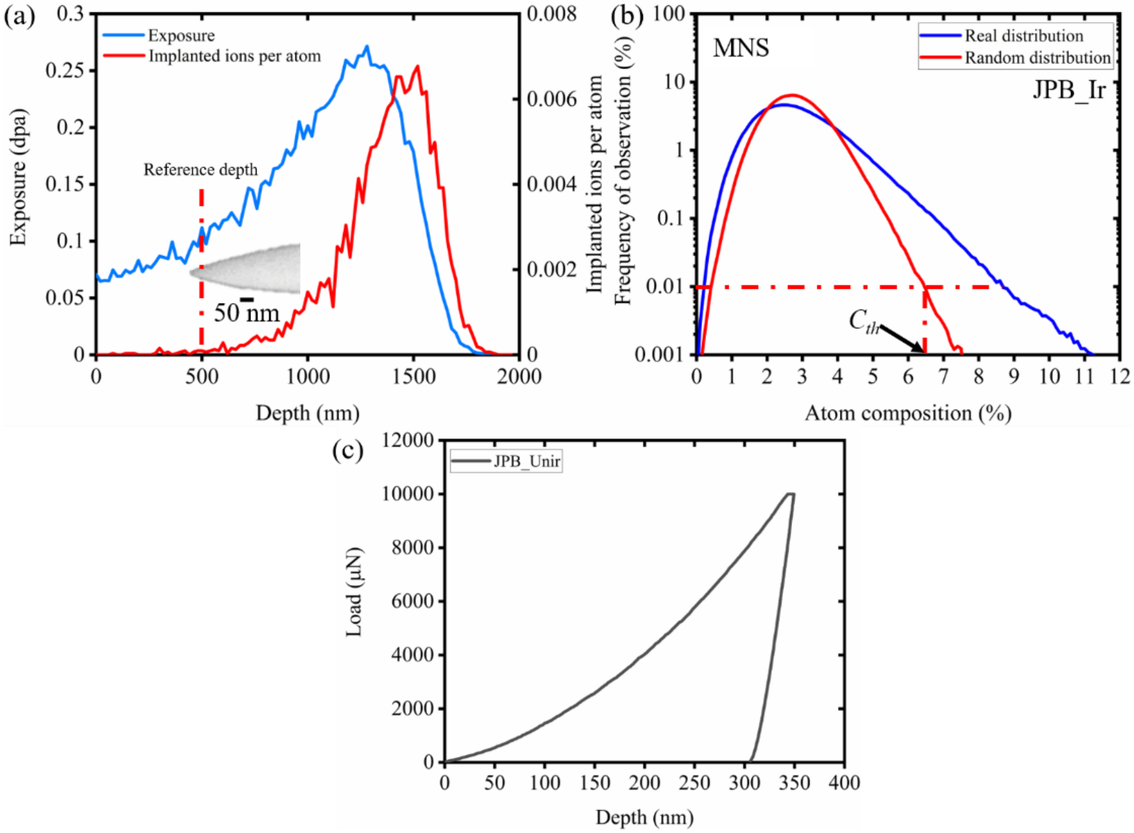

Fig. 1. (a) Damage (in dpa) and implantation (in ion per atom) profiles that were calculated with SRIM using the quick damage method. The reference depth for 0.1 dpa damage is 500 nm. The tip apex was kept at 450 nm from the surface (as can be seen in the figure) so that the 0.1 dpa region could be targeted for APT data acquisitions. (b) An example of an isoposition histogram, taken from the JPB_Ir sample, for MNS-rich clusters. This also illustrates the meaning of the concentration threshold (C_{th}) value. (c) A load vs displacement profile obtained from nanoindentation experiments on the JPB_Unir sample.

2.3. Materials characterisation

2.3.1. Atom probe tomography

APT was performed on CAMECA's LEAP 5000 XR at the GENESIS platform of Groupe de Physique des Matériaux (GPM), Rouen, France. Focused ion beam milling (FIB) was used to prepare tips for APT. Several tips from different positions of the samples were prepared to check the variability in the microstructures. A Zeiss XB540 Crossbeam instrument was used for FIB milling. The cleaning of the tips was performed at 2 kV and 90 pA to minimise the Ga implantation. The tip apex was kept at 450 nm depth (Fig. 1 (a)) after annular milling so that 0.1 dpa region can be analysed during APT data acquisitions. The final diameter of the tip was maintained at less than 100 nm.

The APT acquisitions were made using the voltage mode at 55 K temperature. The pulse fraction and pulse repetition rate were kept at 20 % and 200 kHz, respectively. The detection rate was varied (0.1–0.3 %) during the analysis to keep a constant evaporation flux; as the sample diameter changes during analysis.

The reconstruction of the APT data was carried out in CAMECA's Integrated Visualization and Analysis Software (IVAS; 3.8.10 version). The voltage method was used for reconstruction. The image compression factor value was kept as 1.65. The *k*-factor values were calibrated using the interplanar spacing of low-index crystallographic poles, such as (011), (002), and (222); as observed during analyses. The first few thousand atoms were ignored for the reconstruction because the samples were being aligned during this time and the Ga concentration was also higher at the beginning.

Further data analysis was carried out in GPM 3D data software; developed by the GPM instrumentation team. The mass-to-charge ratio peaks were identified and decomposed using the natural abundance of the elements. The decomposed data were used to calculate the global composition of the samples. The data from all the tips of a particular sample were added to calculate the average composition values, which are reported here. The matrix composition was calculated by creating a new volume of the data without clusters in it.

The isoposition method (IPM) was used to identify the clusters in the unirradiated, irradiated, and post-irradiation-annealed samples. Here, the potentially clustered atoms were first filtered using a composition threshold (C_{th}) value. C_{th} corresponds to the concentration of all solutes considered as core atoms that has a relative occurrence equal to 0.01 % in the randomised APT volume. One such example of the isoposition histogram, indicating the C_{th} value, can be seen in Fig. 1 (b). As the MNS-rich clusters have been reported to be enriched in Mn, Ni, Si, Cu, and P [42, 43]; therefore, all these elements were considered as core atoms to calculate the C_{th}value for finding the MNS-rich clusters. The filtered atoms were then assigned to the clusters based on the atomic distance method, where atoms within the maximum distance (d_{max} = 0.4 nm) value were assigned to the same cluster. This was followed by assigning the minimum number of core atoms (N_{min}) in the clusters. The choice for N_{min} was made in a way that zero clusters were obtained in the random solid solution. Using the C_{th}, d_{max}, and N_{min} values of each volume, three-dimensional (3D) atom maps were produced to highlight the solute rich regions, and are presented here.

Once the clusters were identified, the interface between the clusters and the matrix was defined; to calculate the core composition and the diameter of the clusters. This was done by performing an erosion procedure. Two erosions were performed: The first erosion was performed by keeping the interface at the half maximum of the concentration profile, and the second erosion was performed at the plateau value of the concentration profile. Further information on IPM can be seen in reference [45].

The first erosion data were used to calculate the diameter, number density, and volume fraction of the clusters. The diameter of each cluster was calculated using the expression given in Equation 1.

$$d = 2 \times \sqrt[3]{\frac{3nV_{at}}{4\pi Q}} \tag{1}$$

Here, n is the number of atoms in each cluster, V_{at} is the atomic volume of Fe, and Q is the detection efficiency of LEAP 5000 XR – which is 0.52.

The number density (N) was calculated as the total number of clusters identified over the total volume analysed. The clusters within the volume were counted as full clusters and the clusters at the edges of the volume were counted as half clusters. The total volume (V_T) analysed is given by the expression in Equation 2.

$$V_T = \frac{n_1 \times V_{at}}{Q} \tag{2}$$

Where n_1 is the total number of atoms collected from all the tips of each sample. The volume fraction (f_v) of the clusters is given by Equation 3.

$$f_v = \frac{Total\ number\ of\ atoms\ in\ the\ clusters}{Total\ number\ of\ atoms\ collected} \tag{3}$$

After performing the second erosion, a separate volume containing only cluster cores was saved. The mass over charge peaks obtained from this volume were also treated in the same way as for the bulk volume: The mass over charge peaks were identified and decomposed using the natural abundance of the elements to calculate the cluster composition.

2.3.2. Nanoindentation

The nanoindentation measurements were performed on a TI 950 TriboIndenter from HYSITRON, Bruker. A Berkovich tip was used to perform all the indentation tests that were calibrated on fused silica with known bulk modulus. A basic quasi-static trapezoid load function with a maximum load of 10 mN (corresponding to a contact depth of about 350 nm) and a dwell time of 5 s was used for this work. The loading and unloading times were 5 s, each. A typical load-displacement curve can be seen in Fig. 1 (c) for JPB_Unir. A total of 20 readings were taken for each sample and an average value is presented here. Each indent was separated by a distance of 30 µm from each other; to avoid the interaction between the plastic zones created by each indent. Oliver & Pharr indentation method [46] was used to determine the hardness (H_{IT}) values; with the slope of the unloading curves.

3. Results

3.1. Microstructure

3.1.1. Before and after irradiation

The distribution of the solute atoms (Mn, Ni, Si, Cu, P, and all solutes together (called MNS atom map)) in the volumes obtained from APT, for JPB_Unir, JPC_Unir, JPB_Ir, and JPC_Ir samples, is shown in the atom maps presented in Fig. 2 (a), (b), (c), and (d), respectively. Atoms located in an area enriched in one of these elements or these elements together (MNS) are highlighted using the IPM. The C_{th} and N_{min} values used to identify enriched areas for different elements and five solutes together are presented in Table 3. It can be stated by visual inspection that the irradiation of the samples with 0.1 dpa dose has caused the solutes to cluster. The atom maps for Ni suggest that Ni clusters more in the JPC_Ir sample than in the JPB_Ir sample.

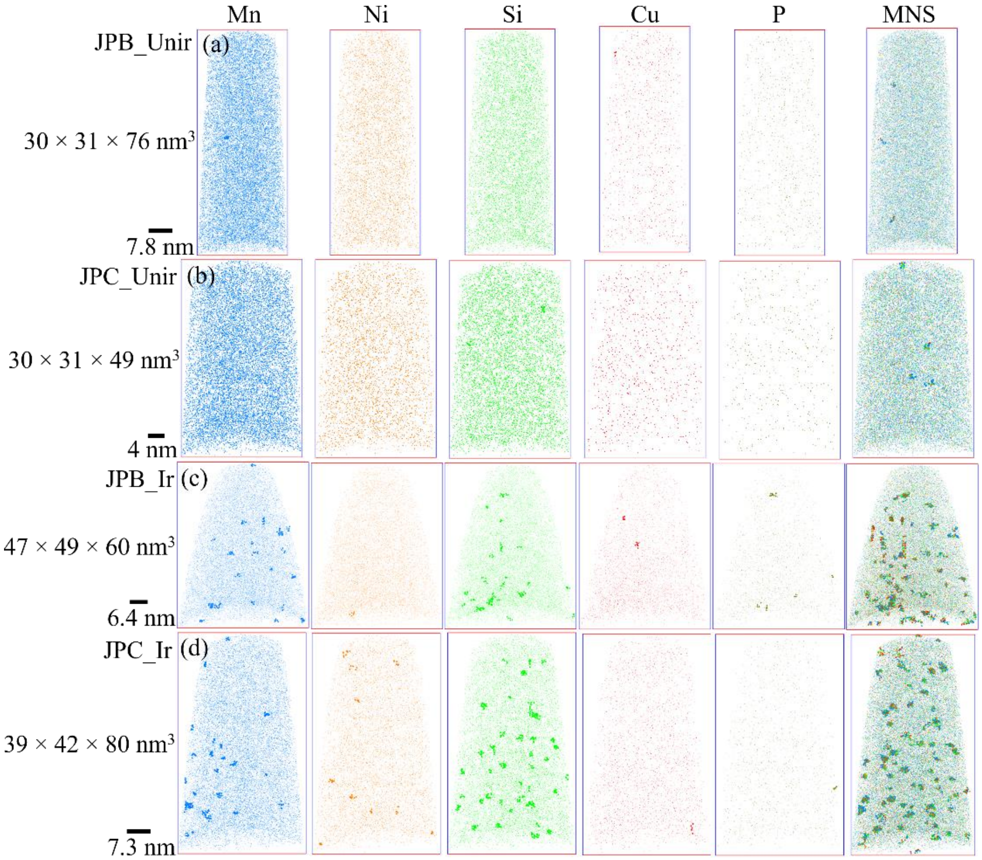

Fig. 2. The atom maps for the (a) JPB_Unir, (b) JPC_Unir, (c) JPB_Ir, and (d) JPC_Ir samples. The irradiation of the samples with 0.1 dpa dose has caused the clustering of all the elements.

Table 3. The C_{th} (%) and N_{min} values for obtaining the atom maps (Fig. 2 and 3) for different elements.

Sample	Elements											
	Mn		Ni		Si		Cu		P		MNS	
	C_{th} (%)	N_{min}	C_{th} (%)	N_{min}	C_{th} (%)	N_{min}	C_{th} (%)	N_{min}	C_{th} (%)	N_{min}	C_{th} (%)	N_{min}
JPB_Unir	4.40	12	2.30	5	2.70	6	1.30	3	1.20	3	6	10
JPC_Unir	4.10	6	2.30	4	2.90	4	1.40	3	1.20	2	5.90	9
JPB_Ir	3.80	6	2.70	7	3.30	10	1.80	5	1.60	3	6.40	11
JPC_Ir	3.80	6	2.40	5	3.00	7	1.60	4	1.40	3	6.10	12
JPB_PIA	3.70	7	2.20	4	2.70	5	1.30	4	1.30	3	5.40	9
JPC_PIA	3.80	6	2.30	5	2.90	4	1.50	4	1.30	3	5.80	6

3.1.2. After post-irradiation annealing

The atom maps obtained for different elements in JPB_PIA and JPC_PIA samples are shown in Fig. 3 (a) and (b), respectively. The C_{th} and N_{min} values for obtaining these atom maps can be seen in Table 3. On visual inspection of JPB_PIA and JPC_PIA samples with respect to JPB_Ir and JPC_Ir samples, respectively, it can be said that the clustering has not disappeared after PIA.

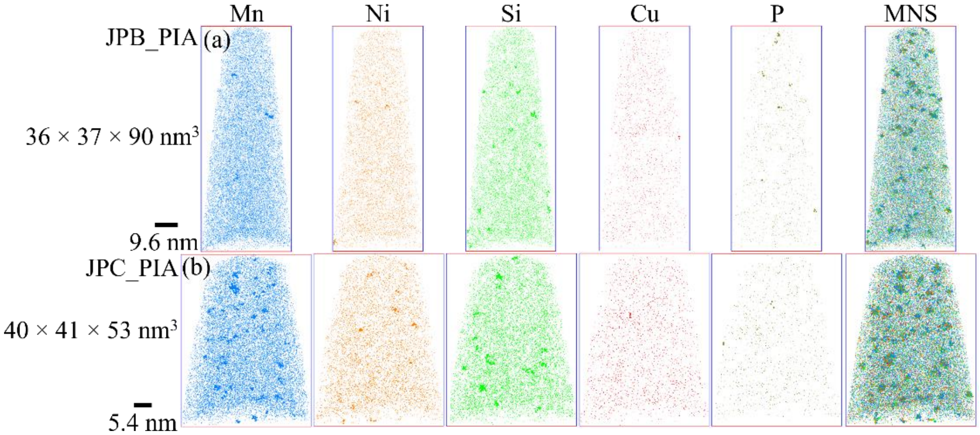

Fig. 3. The atom maps for the (a) JPB_PIA, and (b) JPC_PIA samples. The clustering has not disappeared after the post-irradiation annealing of the samples.

3.2. Solute clustering

It is hard to visually analyse the atom maps (Fig. 2 and 3) to properly understand the clustering of different elements; therefore, a statistical test (V parameter test [34,47]) was performed to understand the clustering carefully. V parameter can help to understand the early clustering of low-concentration elements. It measures the statistical difference between the experimental and the random distribution of the elements. A higher V parameter value qualitatively signifies a higher deviation from the random distribution. V parameters were calculated by summing the difference between the experimental/real (P_i^e) and the random (P_i^r) concentration of the elements distributions as per the relation given in Equation 4.

$$V = \sum_i |P_i^e - P_i^r| \quad (4)$$

Here, the V parameter tests were performed on the data from isoposition histograms (*e.g.*, Fig. 1 (b)) obtained via the IPM.

The V parameters obtained for Mn, Ni, Si, Cu, P, and MNS elements in different volumes of JPB and JPC samples are shown in Fig. 4 (a) and (b), respectively. The average V parameter values for these elements are presented in Table 4. The average values were calculated by summing the $|P_i^e - P_i^r|$ values calculated from isoposition histograms of all the APT volumes of a particular sample. This was done to get the correct representation and information for the bulk of the sample rather than individual volumes. The error bars presented in Table 4 are the standard deviations (SD) – which were calculated by using the expression given in Equation 5.

$$SD = 2 \times \sqrt{\frac{\sum(x-\bar{x})^2}{(z-1)}} \tag{5}$$

Here, x is the single data point ($|P_i^e - P_i^r|$) in the entire dataset, $\bar{x}$ is the mean of the entire dataset, and z is the total number of data points in a particular sample.

Overall, the average V parameter values for the unirradiated samples indicate a deviation from the random distribution; however, relatively higher average V parameter values were obtained for the irradiated samples. This confirms that the irradiation of the samples has caused the clustering of solutes. It is important to mention here that the V parameter values for Mn and Ni in some APT volumes of JPB_Ir were found to be lower than the corresponding V parameter values in JPB_Unir. However, the average V parameter values, representing the information for the bulk sample, for these elements in the JPB_Ir sample are slightly higher than the average V parameter values in the JPB_Unir sample. Not much difference in the average V parameter values of the post-irradiation-annealed samples was found with respect to their irradiated conditions. This indicates that clustering has not disappeared after PIA; as seen in the APT maps in Fig. 3.

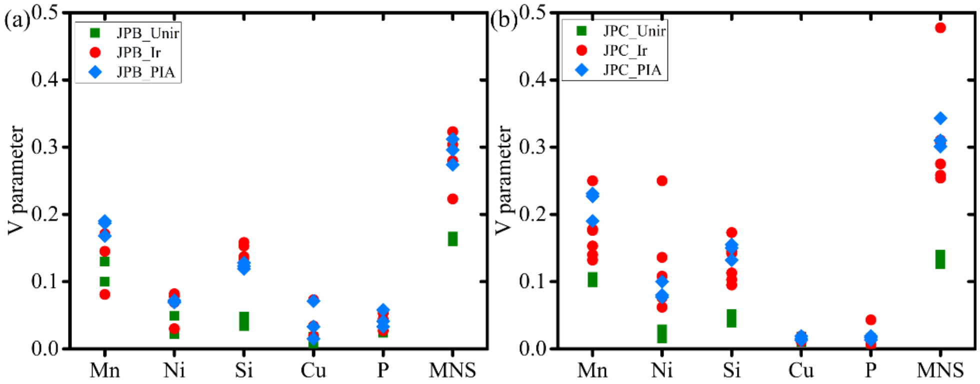

Fig. 4. V parameters, as obtained from isoposition histograms of Mn, Ni, Si, Cu, P, and MNS elements, are shown here for different volumes of (a) JPB and (b) JPC samples under unirradiated, irradiated, and post-irradiation-annealed conditions.

Table 4. The average V parameter values for JPB and JPC samples under unirradiated, irradiated, and post-irradiation-annealed conditions.

Sample	Mn	Ni	Si	Cu	P	MNS
JPB_Unir	0.12 ± 0.0004	0.05 ± 0.0004	0.04 ± 0.0002	0.01 ± 0.0004	0.03 ± 0.0002	0.16 ± 0.0004
JPC_Unir	0.1 ± 0.0004	0.03 ± 0.0002	0.05± 0.0002	0.02 ± 0.0002	0.01 ± 0.0006	0.13 ± 0.0004
JPB_Ir	0.14 ± 0.0004	0.07 ± 0.0004	0.12 ± 0.0004	0.06 ± 0.0006	0.05 ± 0.0002	0.29 ± 0.0006
JPC_Ir	0.17 ± 0.0002	0.12 ± 0.0004	0.14 ± 0.0002	0.02 ± 0.0004	0.02 ± 0.0002	0.31 ± 0.0004
JPB_PIA	0.18 ± 0.0006	0.07 ± 0.0004	0.12 ± 0.0004	0.02 ± 0.0006	0.05 ± 0.0002	0.29 ± 0.0006
JPC_PIA	0.21 ± 0.0006	0.09 ± 0.0004	0.14 ± 0.0006	0.02 ± 0.0008	0.02 ± 0.0002	0.31 ± 0.0008

3.3. Global and matrix chemical compositions

The average global and matrix compositions (in at %) obtained from APT for the irradiated and post-irradiation-annealed samples are shown in Table 5. Table 5 also shows the average global compositions for unirradiated samples. The average global APT composition values for C, V, Mo, and Mn are lesser than the nominal composition values (in brackets in Table 5 or Table 1). In fact, V was not detected in any of the unirradiated samples. This is because these elements are carbide formers [8,10,48], and as APT is a local technique, these variations are thus expected [48]. The average global APT and nominal compositions for Cr are approximately the same. A higher global average APT composition of Ni was measured for all the samples, except JPB_PIA where a lower amount was found. The average global APT composition for Si is slightly higher for JPC_Unir and JPC_Ir, and approximately the same for JPB_Unir, JPB_Ir, JPB_PIA, and JPC_PIA. The APT global compositions for Cu and P are the same as the nominal compositions. These observed differences between the APT and the nominal compositions are expected, as reported previously [48,49]. It is important to note here that the average matrix APT concentration values for Mn, Ni, Si, Cu, and P are lower than their average global APT values. This is because these elements cluster as MNS-rich clusters. Slight differences were observed in the matrix compositions of JPB and JPC samples for Mn, Ni, Si, Cu, and P after PIA with respect to their irradiated conditions.

Table 5. The average global and matrix APT compositions obtained from different tips of JPB and JPC samples under irradiated and PIA conditions are presented in this table. The average global APT compositions for both samples under unirradiated conditions are also shown. In the case of unirradiated samples, global and matrix are the same thing. The nominal compositions are presented in brackets. All the values are in at %.

Code	C	Mn	Si	Cr	Ni	Mo	V	P	Cu
Global APT composition for unirradiated samples									
JPB	0.17± 0.04 (0.92)	1.29 ± 0.2 (1.43)	0.50 ± 0.01 (0.51)	0.15 ± 0.03 (0.16)	0.86 ± 0.02 (0.78)	0.24 ± 0.02 (0.31)	- (0.01)	0.029 ± 0.001 (0.030)	0.010 ± 0.002 (0.009)
JPC	0.29± 0.02 (0.83)	1.12 ± 0.13 (1.46)	0.56 ± 0.02 (0.53)	0.15 ± 0.01 (0.16)	0.82 ± 0.02 (0.77)	0.29 ± 0.01 (0.31)	- (0.01)	0.005 ± 0.002 (0.013)	0.009 ± 0.002 (0.009)
Global APT composition for irradiated samples									
JPB	0.27± 0.12	1.11 ± 0.14	0.52 ± 0.07	0.13 ± 0.03	0.87 ± 0.02	0.27 ± 0.04	0.0003± 0.0002	0.026 ± 0.007	0.008 ± 0.001
JPC	0.39± 0.19	1.08 ± 0.2	0.61 ± 0.04	0.11 ± 0.03	0.87 ± 0.07	0.23 ± 0.03	0.0009± 0.0002	0.006 ± 0.002	0.009 ± 0.004
Matrix APT composition for irradiated samples									
JPB	0.27± 0.12	1.09 ± 0.14	0.51 ± 0.06	0.13 ± 0.03	0.85 ± 0.03	0.27 ± 0.04	0.0003± 0.0002	0.018 ± 0.006	0.007 ± 0.001
JPC	0.39± 0.19	1.04 ± 0.15	0.58 ± 0.06	0.11 ± 0.03	0.83 ± 0.05	0.23 ± 0.03	0.0008± 0.0003	0.004 ± 0.002	0.008 ± 0.003
Global APT composition for post-irradiation-annealed samples									
JPB	0.11± 0.13	0.93 ± 0.07	0.52 ± 0.02	0.14 ± 0.01	0.61 ± 0.07	0.27 ± 0.01	0.0004± 0.0002	0.03 ± 0.006	0.007 ± 0.002
JPC	0.04± 0.01	1.17 ± 0.18	0.53 ± 0.01	0.12 ± 0.03	0.9 ± 0.01	0.23 ± 0.02	0.0007± 0.0002	0.005 ± 0.001	0.008 ± 0.001
Matrix APT composition for post-irradiation-annealed samples									
JPB	0.11± 0.13	0.92 ± 0.07	0.51 ± 0.02	0.14 ± 0.01	0.60 ± 0.07	0.27 ± 0.02	0.0005± 0.0002	0.027 ± 0.005	0.004 ± 0.002
JPC	0.04± 0.01	1.15 ± 0.18	0.51 ± 0.01	0.12 ± 0.03	0.88 ± 0.01	0.23 ± 0.02	0.0007± 0.0002	0.003 ± 0.001	0.006 ± 0.0003

3.4. Cluster information

The variation in the number density, volume fraction, and diameter of MNS-rich clusters in irradiated and post-irradiation-annealed samples can be seen in Fig. 5 (a), (b), and (c), respectively. The figure also illustrates the scatter in the data taken from different tips. The average values for number density, volume fraction, and diameter of the MNS-rich clusters are also shown in Table 6. The average number density and volume fraction increase as the bulk P content decreases, *i.e.*

from sample JPB_Ir to sample JPC_Ir. This is more pronounced for the number density. The average diameter decreases slightly as the bulk P content decreases. The post-irradiation-annealed samples, JPB_PIA and JPC_PIA, show a slight decrease in the number density and the volume fraction when compared with their irradiated conditions, *i.e.* JPB_Ir and JPC_Ir, respectively. The difference is within the error bars. This decrease in the number density and the volume fraction after PIA, if considered notable, also suggests that the clusters are not thermodynamically stable at 350 °C. This has been a debated topic [2,3,21,50] which needs further investigation and is out of the scope of the current work. The average cluster diameter remained approximately the same after PIA.

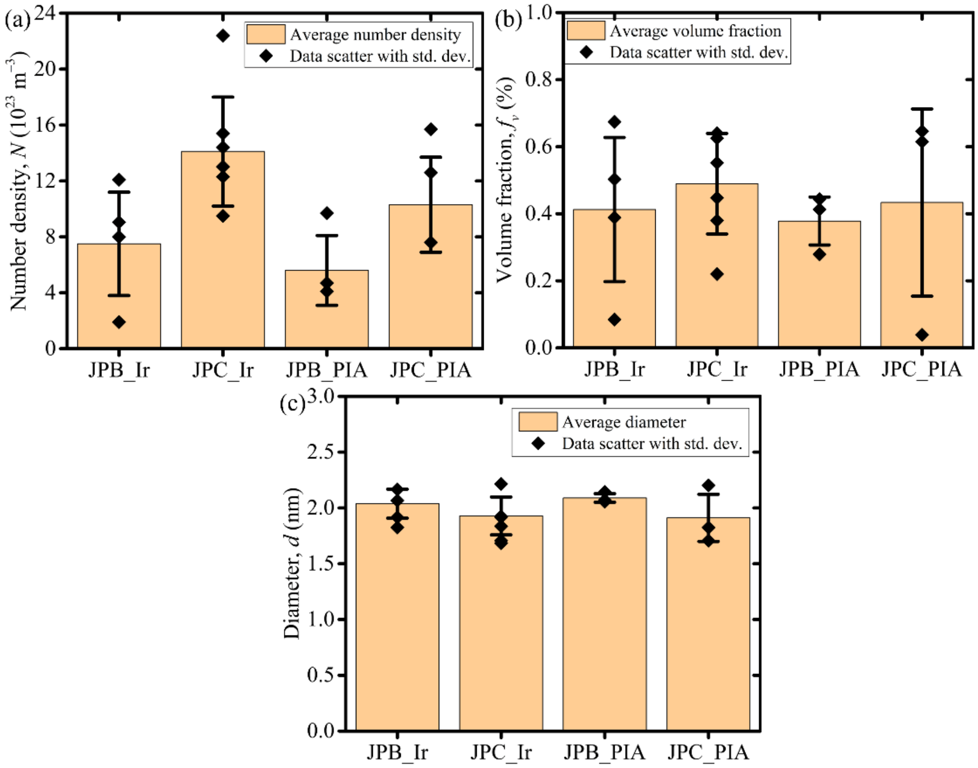

Fig. 5. The variation in the (a) number density, (b) volume fraction, and (c) diameter of MNS-rich clusters in irradiated and post-irradiation-annealed samples.

Table 6. The average values for number density, volume fraction, and diameter of the MNS-rich clusters that were observed in JPB_Ir, JPC_Ir, JPB_PIA, and JPC_PIA samples.

Sample	Number density, N (× 10^{23} m^{-3})	Volume fraction, f_v (%)	Diameter, d (nm)
JPB_Ir	7.5 ± 3.7	0.41 ± 0.21	2.04 ± 0.13
JPC_Ir	14.1 ± 3.9	0.48 ± 0.15	1.92 ± 0.17
JPB_PIA	5.6 ± 2.5	0.37 ± 0.07	2.08 ± 0.03
JPC_PIA	10.3 ± 3.4	0.43 ± 0.27	1.91 ± 0.21

The average cluster composition obtained from irradiated and post-irradiation-annealed samples is shown in Table 7. The error bars in the table are the standard deviations of average cluster compositions from individual APT volumes. The amount of Fe seen in these clusters has been reported [13,48] to be because of the APT artifact; due to the local magnification effect causing trajectory overlap [51]. However, there are chemical composition correction models [52–54] developed by the GPM team that can be used to identify and eventually quantify the introduction of matrix atoms into cluster core due to trajectory aberrations. This will be reported separately as for the current work the idea is to understand the effect of P on the clustering mechanism of MNS-rich clusters.

Table 7. The average cluster compositions for JPB_Ir, JPB_Ir, JPB_PIA, and JPC_PIA samples. All the values are in at %.

Sample	Fe	Mn	Ni	Si	Cr	Mo	Cu	P	C
JPB_Ir	86.74 ± 1.95	4.73 ± 0.12	4.82 ± 0.21	2.58 ± 0.13	0.15 ± 0.04	0.11 ± 0.02	0.26 ± 0.07	0.43 ± 0.17	0.20 ± 0.04
JPC_Ir	83.70 ± 1.56	5.75 ± 0.20	5.99 ± 0.15	4.00 ± 0.21	0.05 ± 0.01	0.10 ± 0.01	0.12 ± 0.02	0.12 ± 0.04	0.17 ± 0.06
JPB_PIA	88.29 ± 2.87	4.16 ± 0.10	3.91 ± 0.09	2.37 ± 0.11	0.11 ± 0.02	0.23 ± 0.08	0.08 ± 0.03	0.70 ± 0.20	0.15 ± 0.05
JPC_PIA	87.53 ± 0.64	4.61 ± 0.11	4.54 ± 0.10	2.81 ± 0.08	0.12 ± 0.02	0.18 ± 0.06	0.09 ± 0.02	0.08 ± 0.02	0.05 ± 0.01

Table 7 shows that the clusters in the JPB_Ir sample, with higher bulk P content, have higher P content (0.43 at %) in the clusters than the clusters (0.12 at %) in the JPC_Ir sample. A higher amount of Cu was observed for the clusters in the JPB_Ir sample (0.26 at %) when compared to the clusters in the JPC_Ir sample (0.12 at %). These observations are suggestive of the synergy between Cu and P. A higher amount of P in the JPB_Ir sample led to a decrease in the Mn (4.73 at %), Ni (4.82 at %), and Si (2.58 at %) concentrations in the clusters than the Mn (5.75 at %), Ni (5.99 at %), and Si (4.00 at %) concentrations in the clusters for JPC_Ir samples. These observations are also true for Mn, Ni, and Si in the post-irradiation-annealed samples. The concentrations of Mn, Ni, and Si in the clusters for both steels decrease after PIA. This could be due to the beginning of the dissolution of the clusters as understood from the decrease in the number density and the volume fraction of MNS-rich clusters after PIA (Fig. 5 and Table 6). The clusters in the JPB_PIA sample show a higher P content (0.70 %) than the clusters in JPC_PIA (0.08 %). The Cu concentrations in the clusters in JPB_PIA and JPC_PIA are 0.15 % and 0.05 %, respectively. The Cu concentration has gone down in the post-irradiation-annealed samples, especially in the JPB_PIA sample.

3.5. Hardness

The hardness (H_{IT}) data as obtained from nanoindentation tests, for unirradiated, irradiated, and post-irradiation-annealed samples, are shown in Table 8. The table also contains data for hardening (the difference between the hardness of unirradiated and irradiated samples) and recovery (the difference between the hardness of irradiated and post-irradiation-annealed samples). The uncertainty values presented in the table for hardening and recovery were calculated using the error propagation method [55]. Note that there is a reasonable agreement between the absolute hardness and the hardening values measured at similar depths by Röder *et al.* [30] on the same samples: the hardening values obtained from current work for the JPB and the JPC samples are approximately the same (~0.72 GPa and ~0.43 GPa for JPB and JPC, respectively) as what was reported on the same samples at 200 nm indentation depth. Higher hardening in the JPB sample, in comparison to the JPC sample, was observed by Röder *et al.* [27] for a larger range of fluences 0.01 to 1 – which is in line with the current observation.

The 10 mN load used in this work led to an indentation depth of approximately 350 nm (Fig. 1 (c)). It has been reported that [56–58] the mechanical properties of the irradiated layer can be separated from the substrate if the indent depth is <0.33 times the thickness of the irradiated layer or between 200-500 nm. Note that there is no standard value for this depth as it should depend on the situation. The irradiated layer in the current case is up to about 1800 nm depth (Fig. 1 (a)), making the indentation depth (~350 nm) about 0.19 times the thickness of the irradiated layer. The indentation depth targeted for the current work is within the recommended limit. Therefore, it can be said that the hardness values obtained for irradiated and post-irradiation-annealed samples represent the effect of irradiation and PIA on hardening and recovery, respectively. However, it has to be pointed out that the damage profile is not homogeneous in this area, and there is implantation of Fe. Thus the hardening is likely to be inhomogenous in the entire irradiated depth.

The irradiated samples show higher hardness than the unirradiated samples; indicating that the formation of radiation-induced features has caused the hardening of the samples. The JPB sample shows a higher hardening than the JPC sample. As the only difference between these samples is in P content then it can be said that the increase in P content in steels leads to an increase in hardening. The JPB sample shows a higher recovery than the JPC sample. This suggests that higher recovery has happened in the sample containing higher P content. The hardening and recovery values are further discussed in the discussion section.

Table 8. The nanoindentation hardness (H_{IT}) data obtained for unirradiated, irradiated, and post-irradiation-annealed samples. The table also shows the hardening and recovery values.

Sample	Average hardness, H_{IT} (GPa)	Standard deviation (SD)/uncertainty
JPB_Unir	3.18	0.27
JPB_Ir	3.91	0.25
JPB_PIA	3.46	0.12
JPC_Unir	2.98	0.09
JPC_Ir	3.48	0.22
JPC_PIA	3.42	0.21
	Hardening (GPa)	
JPB	0.73	0.36
JPC	0.5	0.23
	Recovery (GPa)	
JPB	0.45	0.27
JPC	0.06	0.3

4. Discussion

4.1. Irradiation hardening and post-irradiation annealing effect

It is important to mention here that hardening under ion irradiation is depth-dependent – which makes it difficult to relate the microstructure and the hardness at a given depth. The approach below is of a simplified nature and the results from a single depth were used for this work. The obtained hardness values from nanoindentation tests were converted to the equivalent yield stress (σ_y) values. Rodríguez *et al.* [59] performed high-throughput experimentation to develop the correlation between the yield stress and the hardness for nanoindentation tests; with different indentation depths (50–2000 nm). A linear relation between the yield stress and the hardness values was reported for different types of steel. The relation is given in Equation 6.

$$H_{IT} = b + c'\sigma \tag{6}$$

Where the values of b and c' varied based on the indentation depth. b and c' values were reported to be 0.16 GPa and 5.16, respectively, when the indentation depth was more than 250 nm, as in the current work. This same relation was also used by Tao *et al.* [60] for converting nanohardness values of duplex stainless steel to yield stress. Based on the same relation, the yield stress values were calculated for the current work and are presented in Table 9. Note that such property–property conversions involve some degree of uncertainty. However, the relation used here for this property–property conversions is derived from high-throughput experimentation on different materials, as mentioned above. In addition, the yield stress values estimated for the JPB and the JPC samples in the unirradiated condition agree reasonably well with the measured yield stress values (511 MPa and 497 MPa for JPB and JPC, respectively) in the unirradiated condition, reported by Röder *et al.* [30]. Hence, it is safe to state that the method used for estimating the yield stress values can be reasonably accepted.

Table 9. The estimated values of yield stress (in MPa) from the hardness data. The uncertainty values were calculated based on the error propagation method.

Sample	Yield stress, σ_y (MPa)	Uncertainty
JPB_Unir	500	52
JPB_Ir	641	48
JPB_PIA	554	23
JPC_Unir	462	17
JPC_Ir	558	42
JPC_PIA	546	39

Subsequently, the hardening ($\Delta\sigma_y$) of the samples due to irradiation was calculated, where $\Delta\sigma_y$ refers to the yield stress difference between the irradiated and the unirradiated samples. The obtained hardening results are plotted in Fig. 6 (a). The decrease in the hardening values, *i.e.* recovery, due to PIA can also be seen in Fig 6 (b). Note that Bergner *et al.* [32] reported an increase in the measured yield stress values of about 223 MPa and 197 MPa for the JPB and the JPC samples, respectively, after a neutron dose of 0.133 dpa. The estimated increase in yield stress values in the current work, after an ion dose of 0.1 dpa, were found to be 141 MPa and 96 MPa for the JPB and the JPC samples, respectively. The observed differences in the properties from these works are likely because of the irradiation dose and the source of irradiation (neutron vs ion) – but the trend is the same as observed in the current work. This is another indication that our property-property conversion method is reasonably correct.

A theoretical equivalent of hardening and recovery values was calculated for comparison purposes and the data is shown in Fig. 6. Hardening in the material is a consequence of several contributing factors, such as dislocations and carbides, and Hall-Petch contribution. According to Monnet *et al.* [61], the quadratic sum of the contributions of the carbides, the dislocation forest, and the solute clusters to the critical resolved shear stress (CRSS) result in the following expression (Equation 7) for irradiation hardening in RPV steels:

$$\Delta\sigma = M(\sqrt{\tau_{forest}^2 + \tau_{carbide}^2 + \tau_{sc}^2} - \sqrt{\tau_{forest}^2 + \tau_{carbide}^2}\,) \qquad (7)$$

where τ_{forest} is the CRSS contribution of the dislocation forest, $\tau_{carbide}$ is the CRSS contribution of the carbides and τ_{sc} is the CRSS contribution of the solute clusters. M is Taylor's factor whose value is 3.05. Since the exact information about carbides and dislocation forests was not available for this work; therefore, the τ_{forest} and $\tau_{carbide}$ were adapted from the typical values of these components for RPV steels from reference [62]. The values are 62 MPa and 36 MPa, respectively. The Dispersed Barrier Hardening model was used to calculate the CRSS contribution of the solute clusters (τ_{sc}) [63]. The model is given by the relation in Equation 8.

$$\tau_{sc} = \alpha_{sc}\mu b\sqrt{Nd} \qquad (8)$$

Where α_{sc} is the obstacle strength, μ is the shear modulus of the material, b is the Burgers vector and d is the cluster diameter. Here, the values for μ and b were taken as 83 GPa [64] and 0.248 nm, respectively. To estimate the value of α_{sc}, it was assumed that no SIA clusters were present in the JPC sample as very little recovery was seen (Table 8) for the JPC sample, *i.e.* the hardening can be fully described by Equation 7. Based on this assumption, α_{sc} value was varied until the experimental and theoretical hardening values matched. The α_{sc} value was found to be 0.068 – which was used to calculate the theoretical hardening values for the other samples. This value is approximately the same (0.066 ± 0.006) as what was estimated by Ulbricht *et al.* [65] for MNS-rich clusters in RPV steels.

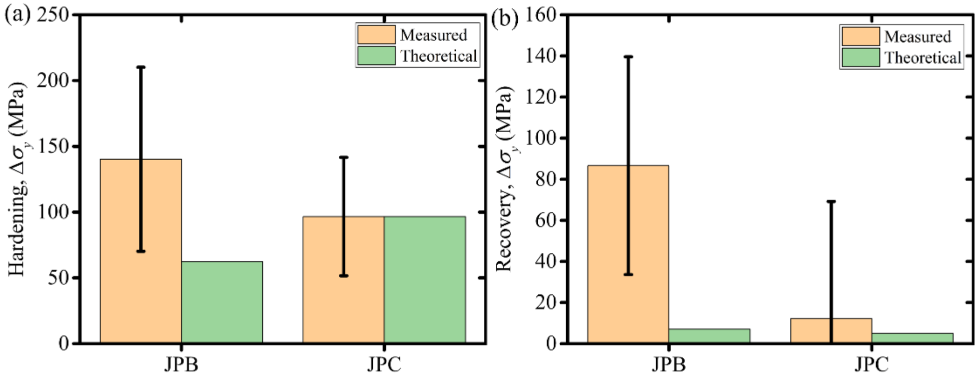

Fig. 6. The (a) hardening due to irradiation and (b) recovery due to post-irradiation annealing for JPB and JPC samples. The uncertainty values here were calculated using the error propagation method.

The theoretical hardening value obtained for the JPB sample by using Equation 7 and α_{sc} = 0.068 is lower than the experimental value. This suggests that apart from the hardening contribution from carbides, dislocations, and solute clusters, we also have the contribution from matrix damage due to irradiation. This observation is in agreement with the stabilisation of small SIA clusters by P (not visible to APT); as explained previously [31,62]. A higher amount of recovery in the hardening was observed for JPB samples when compared to the JPC sample. The recovery as per the theoretical calculations (due to the dissolution of the clusters) showed a very low value when compared to the measured value for the JPB sample. The difference in recovery between the theoretical and the experimental values for the JPB sample could be explained by the dissolution of the small SIA clusters stabilised by P atoms. The recovery in the JPC sample is partly due to the partial dissolution of the clusters. The differences between the experimental and theoretical recovery, and the difference between the experimental and theoretical hardening for the JPB sample were found to be ~ 79 MPa and ~78 MPa, respectively. These values are approximately the same. These values are suggestive of the fact that the extra hardening was because of the presence of stabilised SIA clusters which were dissolved after PIA; leading to higher recovery in the JPB sample. Hence these observations help in rationalising that the P content does stabilise the SIA clusters that act as the nucleation site for the formation of MNS-rich clusters [31].

4.2. Effect of phosphorous

The APT results (Fig. 2, Fig. 4, Table 4, and Table 7) clearly show that the P atoms cluster due to ion irradiation of 0.1 dpa. Gómez-Ferrer *et al.* [34] and Gueye *et al.* [66] have also reported that P-rich clusters can form in Fe-Cr alloys with a low dose of 0.1 dpa. The Mn, Ni, and Si content of the clusters reduced (Table 7) in the presence of higher bulk P content. The higher amount of P in the steel led to a higher amount of Cu in the clusters; suggesting a synergy between Cu and P. Kamboj *et al.* [67] have also reported that in high-P steels, Cu and P nucleate early and provide nucleation sites for the solute clusters.

Although the number density and the volume fraction of the MNS-rich clusters decreased with the increase in the P content in the JPB sample, the JPB sample showed higher hardening than the JPC sample (Fig. 6). The theoretical hardening value calculated using Equation 7 does not equate to the measured hardening value. This reveals that there is another contributing factor to hardening apart from the contribution of carbides, dislocation forest, and solute clusters. Röder *et al.* [30]

hypothesised that this contribution is from the stabilisation of the cascade remnants, whereas Castin *et al.* [31] reported that the P atoms stabilise the SIA clusters – which are created in the material after the displacement cascades. The trapping capability depends on the elastic strain generated due to solute/lattice misfit and solute-SIA cluster bonding. It has been found that the presence of undersized substitutional P atoms leads to lattice contraction [68]. In addition, the P atoms have the strongest segregation tendency, as reported experimentally by Gómez-Ferrer *et al.* [34] and via modelling by Messina *et al.* [69,70], and P atoms have a strong positive flux coupling with self-interstitials and vacancies [71,72]. This negatively impacts the migration energy of the SIA clusters [73]; hence, stabilising them. These stabilised features act as nucleation sites that are enriched by the relatively slow diffusing elements, such as Mn, Ni, and Si [34]; leading to the formation of MNS-rich clusters. The early clustering of P atoms acting as the nucleation site for the solute cluster formation in the Cu-free steels was also observed by Kamboj *et al.* [67] through their APT work. Gueye *et al.* [66] also showcased for high-P containing Fe-Cr alloys that clusters are first enriched with P followed by Ni and Si. A higher recovery in the JPB sample after PIA, where approximately similar differences between the experimental and theoretical recovery (~ 79 MPa), and the experimental and theoretical hardening (~78 MPa) for the JPB sample indicated that the recovery is due to the dissolution of these SIA clusters. Although the SIA clusters are not visible to the APT, it is proposed, from the above observations, that the P atoms do stabilise the SIA clusters which then act as the nucleation sites for the formation of embrittling MNS-rich clusters in RPV steels.

It is also important to mention here that the PIA of the samples indicates that the MNS-rich clusters seem to be not thermodynamically stable at 350 °C. This is understood from the slight reduction in the number density (Fig. 5 (a)) and the volume fraction (Fig. 5 (b)) of the MNS-rich clusters. The cluster composition values (Table 7) after PIA are in support of the fact that cluster enrichment goes down after PIA; indicating a possible start of the dissolution of the clusters.

5. Conclusions

This paper reports the results on understanding the influence of P on the formation of MNS-rich clusters and irradiation hardening in RPV model steels. The APT and nanoindentation results led to the following conclusions:

- The increase in the bulk P content does not result in strong differences in solute cluster characteristics. In the high P steel, a slight decrease in the number density and the volume fraction, and a slight increase in the size of the MNS-rich clusters was observed.
- However, the hardening increased significantly with an increase in bulk P content. This higher hardening was attributed to the stabilisation by P of small self-interstitial atoms (SIA) clusters, not visible to APT.
- A higher amount of P was found in the clusters for samples having higher bulk P content. The higher bulk P content also led to the higher Cu content in the clusters; indicating synergy between Cu and P.
- The post-irradiation annealing of the samples led to a slight decrease in the number density of solute clusters; suggesting that they are unstable at 350 °C and start to dissolve.
- The partial dissolution of solute clusters during PIA is not sufficient to explain the hardness recovery in particular in the high P steel. This confirms that hardening in high P steel is partly due to small SIA clusters invisible to APT.

Acknowledgments

Experiments were performed on GENESIS platform instruments supported by the Région Haute-Normandie, the Métropole Rouen Normandie, CNRS via LABEX EMC^3, and the French National Research Agency via "Investissements d'avenir" program (ANR-11-EQPX-0020). The reported research was performed in the framework of the EU project SOTERIA. This project has received funding from the Euratom research and training programme 2014-2018 under grant agreement n°661913. DS would like to acknowledge Mr. Fabien Cuvilly, Dr. Ivan Blum, and Dr. Aidar Zakirov for their time with training and discussion on SEM-FIB and APT. The use of the HZDR Ion Beam Center facilities and the support of its staff is gratefully acknowledged.

References

[1] M. Kolluri, P. ten Pierick, T. Bakker, B.T. Straathof, A.J. Magielsen, Z. Szaraz, E. D'Agata, C. Ohms, O. Martin, Influence of Ni-Mn contents on the embrittlement of PWR RPV model steels irradiated to high fluences relevant for LTO beyond 60 years, J. Nucl. Mater. 553 (2021).

[2] G.R. Odette, N. Almirall, P.B. Wells, T. Yamamoto, Precipitation in reactor pressure vessel steels under ion and neutron irradiation: On the role of segregated network dislocations, Acta Mater. 212 (2021) 116922.

[3] B.M. Jenkins, P.D. Styman, N. Riddle, P.A.J. Bagot, M.P. Moody, G.D.W. Smith, J.M. Hyde, Observation of Mn-Ni-Si-rich features in thermally-aged model reactor pressure vessel steels, Scr. Mater. 191 (2021) 126–130.

[4] S. Rouland, B. Radiguet, P. Pareige, Investigating radiation-induced segregation on intragranular defects in a 316L(N), J. Nucl. Mater. 557 (2021).

[5] P. Pareige, P. Auger, P. Bas, D. Blavette, Direct observation of copper precipitation in a neutron irradiated FeCu alloy by 3D atomic tomography, Scr. Metall. Mater. 33 (1995) 1033–1036.

[6] G.R. Odette, On the dominant mechanism of irradiation embrittlement of reactor pressure vessel steels, Scr. Metall. 17 (1983) 1183–1188.

[7] E. Meslin, M. Lambrecht, M. Hernández-Mayoral, F. Bergner, L. Malerba, P. Pareige, B. Radiguet, A. Barbu, D. Gómez-Briceño, A. Ulbricht, A. Almazouzi, Characterization of neutron-irradiated ferritic model alloys and a RPV steel from combined APT, SANS, TEM and PAS analyses, J. Nucl. Mater. 406 (2010) 73–83.

[8] P. Auger, M. Akamatsu, D. Blavette, APFIM investigation of clustering in neutron-irradiated Fe-Cu alloys and pressure vessel steels, J. Nucl. Mater. 225 (1995) 225–230.

[9] P.D. Styman, J.M. Hyde, D. Parfitt, K. Wilford, M.G. Burke, C.A. English, P. Efsing, Post-irradiation annealing of Ni-Mn-Si-enriched clusters in a neutron-irradiated RPV steel weld using Atom Probe Tomography, J. Nucl. Mater. 459 (2015) 127–134.

[10] P. Pareige, J.C. Van Duysen, P. Auger, An APFIM study of the microstructure of a ferrite alloy after high fluence neutron irradiation, Appl. Surf. Sci. 67 (1993) 342–347.

[11] A. Ulbricht, J. Böhmert, H.W. Viehrig, Microstructural and mechanical characterization of radiation effects in model reactor pressure vessel steels, ASTM Spec. Tech. Publ. 1475 STP (2006) 151–164.

[12] A. Ulbricht, F. Bergner, J. Böhmert, M. Valo, M.H. Mathon, A. Heinemann, SANS response of VVER440-type weld material after neutron irradiation, post-irradiation annealing and reirradiation, Philos. Mag. 87 (2007) 1855–1870.

[13] P.D. Edmondson, C.M. Parish, R.K. Nanstad, Using complimentary microscopy methods to examine Ni-Mn-Si-precipitates in highly-irradiated reactor pressure vessel steels, Acta Mater. 134 (2017) 31–39.

[14] N. Almirall, P.B. Wells, S. Pal, P.D. Edmondson, T. Yamamoto, K. Murakami, G.R. Odette, The mechanistic implications of the high temperature, long time thermal stability of nanoscale Mn-Ni-Si precipitates in irradiated reactor pressure vessel steels, Scr. Mater. 181 (2020) 134–139.

[15] N. Almirall, P.B. Wells, H. Ke, P. Edmondson, D. Morgan, T. Yamamoto, G.R. Odette, On the elevated temperature thermal stability of nanoscale Mn-Ni-Si precipitates formed at lower temperature in highly irradiated reactor pressure vessel steels, Sci. Rep. 9 (2019) 1–12.

[16] L. Liu, K. Nishida, K. Dohi, A. Nomoto, N. Soneda, K. Murakami, Z. Li, D. Chen, N. Sekimura, Effects of solute elements on hardening and microstructural evolution in neutron-irradiated and thermally-aged reactor pressure vessel model alloys, J. Nucl. Sci. Technol. 53 (2016) 1546–1553.

[17] M.K. Miller, K.A. Powers, R.K. Nanstad, P. Efsing, Atom probe tomography characterizations of high nickel, low copper surveillance RPV welds irradiated to high fluences, J. Nucl. Mater. 437 (2013) 107–115.

[18] P. Auger, P. Pareige, S. Welzel, J.C. Van Duysen, Synthesis of atom probe experiments on irradiation-induced solute segregation in French ferritic pressure vessel steels, J. Nucl. Mater. 280 (2000) 331–344.

[19] P. Pareige, R.E. Stoller, K.F. Russell, M.K. Miller, Atom probe characterization of the microstructure of nuclear pressure vessel surveillance materials after neutron irradiation and after annealing treatments, 249 (2008) 165–174.

[20] A. Ulbricht, F. Bergner, C.D. Dewhurst, A. Heinemann, Small-angle neutron scattering study of post-irradiation annealed neutron irradiated pressure vessel steels, J. Nucl. Mater. 353 (2006) 27–34.

[21] L.T. Belkacemi, E. Meslin, J.P. Crocombette, B. Radiguet, F. Leprêtre, B. Décamps, Striking effect of solute elements (Mn, Ni) on radiation-induced segregation/precipitation in iron-based model alloys, J. Nucl. Mater. 548 (2021).

[22] B.M. Jenkins, J.O. Douglas, N. Almirall, N. Riddle, P.A.J. Bagot, J.M. Hyde, G.R. Odette, M.P. Moody, The effect of composition variations on the response of steels subjected to high fluence neutron irradiation, Materialia. 11 (2020) 100717.

[23] N. Almirall, P.B. Wells, T. Yamamoto, K. Wilford, T. Williams, N. Riddle, G.R. Odette, Precipitation and hardening in irradiated low alloy steels with a wide range of Ni and Mn compositions, Acta Mater. 179 (2019) 119–128.

[24] C.H. Lee, R. Kasada, A. Kimura, B.S. Lee, D.W. Suh, H.C. Lee, Effect of nickel content on the neutron irradiation embrittlement of Ni-Mo-Cr steels, Met. Mater. Int. 19 (2013) 1203–1208.

[25] M.K. Miller, Atom probe tomography characterization of solute segregation to dislocations and interfaces, J. Mater. Sci. 41 (2006) 7808–7813.

[26] Y. Guo, M. Wang, K. Wang, S.H. Song, Relation of embrittlement to phosphorus grain-boundary segregation for an advanced Ni–Cr–Mo RPV steel, J. Mater. Res. Technol. 18

(2022) 2240–2249.

[27] S. V. Fedotova, E.A. Kuleshova, D.A. Maltsev, M.A. Saltykov, Complex study of grain boundary segregation in long-term irradiated reactor pressure vessel steels, J. Nucl. Mater. 528 (2020) 151865.

[28] Y. Nishiyama, T.E. Bloomer, J. Kameda, Effect of bulk phosphorus content on hardening, non-equilibrium segregation and embrittlement in neutron irradiated iron-based alloys, Mater. Res. Soc. Symp. 650 (2001) R6.10.1-R6.10.6.

[29] C.Y. Hsu, J. Stodolna, P. Todeschini, F. Delabrouille, B. Radiguet, F. Christien, Accurate quantification of phosphorus intergranular segregation in iron by STEM-EDX, Micron. 153 (2022) 103175.

[30] F. Röder, C. Heintze, S. Pecko, S. Akhmadaliev, F. Bergner, A. Ulbricht, E. Altstadt, Nanoindentation of ion-irradiated reactor pressure vessel steels–model-based interpretation and comparison with neutron irradiation, Philos. Mag. 98 (2018) 911–933.

[31] N. Castin, G. Bonny, A. Bakaev, F. Bergner, C. Domain, J.M. Hyde, L. Messina, B. Radiguet, L. Malerba, The dominant mechanisms for the formation of solute-rich clusters in low-Cu steels under irradiation, Mater. Today Energy. 17 (2020) 100472.

[32] F. Bergner, A. Ulbricht, H.W. Viehrig, Acceleration of irradiation hardening of low-copper reactor pressure vessel steel observed by means of SANS and tensile testing, Philos. Mag. Lett. 89 (2009) 795–805.

[33] G.R. Odette, T. Yamamoto, T.J. Williams, R.K. Nanstad, C.A. English, On the history and status of reactor pressure vessel steel ductile to brittle transition temperature shift prediction models, J. Nucl. Mater. 526 (2019) 151863.

[34] B. Gómez-Ferrer, C. Heintze, C. Pareige, On the role of Ni, Si and P on the nanostructural evolution of FeCr alloys under irradiation, J. Nucl. Mater. 517 (2019) 35–44.

[35] Y. Dong, A. Etienne, A. Frolov, S. Fedotova, K. Fujii, K. Fukuya, C. Hatzoglou, E. Kuleshova, K. Lindgren, A. London, A. Lopez, S. Lozano-Perez, Y. Miyahara, Y. Nagai, K. Nishida, B. Radiguet, D.K. Schreiber, N. Soneda, M. Thuvander, T. Toyama, J. Wang, F. Sefta, P. Chou, E.A. Marquis, Atom probe tomography interlaboratory study on clustering analysis in experimental data using the maximum separation distance approach M&m 2019, (2019) 1–21.

[36] J.M. Hyde, G. Dacosta, C. Hatzoglou, H. Weekes, B. Radiguet, P.D. Styman, F. Vurpillot, C. Pareige, A. Etienne, G. Bonny, N. Castin, L. Malerba, P. Pareige, Analysis of Radiation Damage in Light Water Reactors: Comparison of Cluster Analysis Methods for the Analysis of Atom Probe Data, Microsc. Microanal. 23 (2017) 366–375.

[37] J.M. Hyde, M.G. Burke, B. Gault, D.W. Saxey, P. Styman, K.B. Wilford, T.J. Williams, Atom probe tomography of reactor pressure vessel steels: An analysis of data integrity, Ultramicroscopy. 111 (2011) 676–682.

[38] J.M. Hyde, E.A. Marquis, K.B. Wilford, T.J. Williams, A sensitivity analysis of the maximum separation method for the characterisation of solute clusters, Ultramicroscopy. 111 (2011) 440–447.

[39] S.H. Kim, T.A. Taiwo, B.W. Dixon, The Carbon Value of Nuclear Power Plant Lifetime Extensions in the United States, Nucl. Technol. 208 (2022) 775–793.

[40] J.F. Ziegler, M.D. Ziegler, J.P. Biersack, SRIM - The stopping and range of ions in matter (2010), Nucl. Instruments Methods Phys. Res. Sect. B Beam Interact. with Mater. Atoms. 268 (2010) 1818–1823.

[41] R.E. Stoller, M.B. Toloczko, G.S. Was, A.G. Certain, S. Dwaraknath, F.A. Garner, On the use of SRIM for computing radiation damage exposure, Nucl. Instruments Methods Phys. Res. Sect. B Beam Interact. with Mater. Atoms. 310 (2013) 75–80.

[42] P.B. Wells, The Character, Stability and Consequences of Mn-Ni-Si Precipitates in Irradiated Reactor Pressure Vessel Steels, University of Claifornia, Santa Barbara, 2016.

[43] P. Auger, P. Pareige, M. Akamatsu, J.C. Van Duysen, Microstructural characterization of atom clusters in irradiated pressure vessel steels and model alloys, J. Nucl. Mater. 211 (1994) 194–201.

[44] S. Shu, P.B. Wells, N. Almirall, G.R. Odette, D.D. Morgan, Thermodynamics and kinetics of core-shell versus appendage co-precipitation morphologies: An example in the Fe-Cu-Mn-Ni-Si system, Acta Mater. 157 (2018) 298–306.

[45] W. Lefebvre-Ulrikson, F. Vurpillot, X. Sauvage, Atom Probe Tomography, London (UK), Academic Press, 2016.

[46] W.C. Oliver, G.M. Pharr, Measurement of hardness and elastic modulus by instrumented indentation: Advances in understanding and refinements to methodology. Journal of Materials Research 19, 3–20 (2004).

[47] D. Blavette, G. Grancher, A. Bostel, L.D.M. Ionique, C. Ua-, F. Sciences, D. Rouen, F.-M. Cedex, F.-M. Cedex, Features From Frequency Distributions for Finely Dispersed Systems, J. Phys. (1988) 433–438.

[48] P.B. Wells, T. Yamamoto, B. Miller, T. Milot, J. Cole, Y. Wu, G.R. Odette, Evolution of manganese-nickel-silicon-dominated phases in highly irradiated reactor pressure vessel steels, Acta Mater. 80 (2014) 205–219.

[49] G.R. Odette, G.E. Lucas, Recent progress in understanding reactor pressure vessel steel embrittlement, Rad. Eff. Defects in Solids 144 (1998) 189–231.

[50] E.A. Kuleshova, G.M. Zhuchkov, S. V. Fedotova, D.A. Maltsev, A.S. Frolov, I. V. Fedotov, Precipitation kinetics of radiation-induced Ni-Mn-Si phases in VVER-1000 reactor pressure vessel steels under low and high flux irradiation, J. Nucl. Mater. 553 (2021) 153091.

[51] F. Vurpillot, A. Bostel, D. Blavette, Trajectory overlaps and local magnification in three-dimensional atom probe, Appl. Phys. Lett. 76 (2000) 3127–3129.

[52] C. Hatzoglou, B. Radiguet, F. Vurpillot, P. Pareige, A chemical composition correction model for nanoclusters observed by APT - Application to ODS steel nanoparticles, J. Nucl. Mater. 505 (2018) 240–248.

[53] C. Hatzoglou, B. Radiguet, P. Pareige, Experimental artefacts occurring during atom probe tomography analysis of oxide nanoparticles in metallic matrix : Quantification and

correction, J. Nucl. Mater. 492 (2017) 279–291.

[54] C. Hatzoglou, B. Radiguet, G. Da, P. Pareige, M. Roussel, M. Hernandez-mayoral, C. Pareige, Quanti fi cation of APT physical limitations on chemical composition of precipitates in Fe e Cr alloys, J. Nucl. Mater. 522 (2019) 64–73.

[55] A. Singh, P. Chaturvedi, Error Propagation, Resonance. 26 (2021) 853–861.

[56] C.K. Dolph, D.J. da Silva, M.J. Swenson, J.P. Wharry, Plastic zone size for nanoindentation of irradiated Fe—9%Cr ODS, J. Nucl. Mater. 481 (2016) 33–45.

[57] T. Miyazawa, T. Nagasaka, R. Kasada, Y. Hishinuma, T. Muroga, H. Watanabe, T. Yamamoto, S. Nogami, M. Hatakeyama, Evaluation of irradiation hardening of ion-irradiated V-4Cr-4Ti and V-4Cr-4Ti-0.15Y alloys by nanoindentation techniques, J. Nucl. Mater. 455 (2014) 440–444.

[58] R. Kasada, S. Konishi, K. Yabuuchi, S. Nogami, M. Ando, D. Hamaguchi, H. Tanigawa, Depth-dependent nanoindentation hardness of reduced-activation ferritic steels after MeV Fe-ion irradiation, Fusion Eng. Des. 89 (2014) 1637–1641.

[59] R. Rodríguez, I. Gutierrez, Correlation between nanoindentation and tensile properties influence of the indentation size effect, Mater. Sci. Eng. A. 361 (2003) 377–384.

[60] P. Tao, J. ming Gong, Y. fei Wang, Y. Jiang, Y. Li, W. wei Cen, Characterization on stress-strain behavior of ferrite and austenite in a 2205 duplex stainless steel based on nanoindentation and finite element method, Results Phys. 11 (2018) 377–384.

[61] G. Monnet, Multiscale modeling of irradiation hardening: Application to important nuclear materials, J. Nucl. Mater. 508 (2018) 609–627.

[62] H. Watanabe, S. Arase, T. Yamamoto, P. Wells, T. Onishi, G.R. Odette, Hardening and microstructural evolution of A533b steels irradiated with Fe ions and electrons, J. Nucl. Mater. 471 (2016) 243–250.

[63] F. Bergner, C. Pareige, M. Hernández-Mayoral, L. Malerba, C. Heintze, Application of a three-feature dispersed-barrier hardening model to neutron-irradiated Fe-Cr model alloys, J. Nucl. Mater. 448 (2014) 96–102.

[64] G. Ghosh, G.B. Olson, The isotropic shear modulus of multicomponent Fe-base solid solutions, Acta Mater. 50 (2002) 2655–2675.

[65] A. Ulbricht, J. Dykas, P. Chekhonin, E. Altstadt, F. Bergner, Small-angle neutron scattering study of neutron-irradiated and post-irradiation annealed VVER-1000 reactor pressure vessel weld material, Front. Nucl. Eng. 2 (2023) 1–12.

[66] P.M. Gueye, B. Gómez-Ferrer, C. Kaden, C. Pareige, Role of Ni, Si and P on the formation of solute-rich clusters under irradiation in Fe-Cr alloys, J. Nucl. Mater. 570 (2022) 153958.

[67] A. Kamboj, M.N. Bachhav, M. Dubey, N. Almirall, T. Yamamoto, E.A. Marquis, G.R. Odette, The effect of phosphorus on precipitation in irradiated reactor pressure vessel (RPV) steels, J. Nucl. Mater. 585 (2023) 154614.

[68] P.H. Warren, C.D. Clement, C. Yang, A. Sen, W.Y. Chen, Y. Wu, L. Wang, J.P. Wharry,

The role of Cr, P, and N solutes on the irradiated microstructure of bcc Fe, J. Nucl. Mater. 583 (2023) 154531.

[69] L. Messina, M. Nastar, T. Garnier, C. Domain, P. Olsson, Exact ab initio transport coefficients in bcc Fe-X (X=Cr, Cu, Mn, Ni, P, Si) dilute alloys, Phys. Rev. B - Condens. Matter Mater. Phys. 90 (2014) 1–15.

[70] L. Messina, T. Schuler, M. Nastar, M.C. Marinica, P. Olsson, Solute diffusion by self-interstitial defects and radiation-induced segregation in ferritic Fe–X (X=Cr, Cu, Mn, Ni, P, Si) dilute alloys, Acta Mater. 191 (2020) 166–185.

[71] E. Meslin, C.C. Fu, A. Barbu, F. Gao, F. Willaime, Theoretical study of atomic transport via interstitials in dilute Fe-P alloys, Phys. Rev. B - Condens. Matter Mater. Phys. 75 (2007) 1–8.

[72] C. Domain, C.S. Becquart, Diffusion of phosphorus in α-Fe: An ab initio study, Phys. Rev. B - Condens. Matter Mater. Phys. 71 (2005) 1–13.

[73] Y. Satoh, T. Yoshiie, S. Arai, Undersize solute element effects on defect structure development in copper under electron irradiation, Philos. Mag. 98 (2018) 646–672.